

# Fundamental Studies Towards Rotor Simulations and Design

Feilin Jia\* and Philippe Spalart†  
*Flexcompute Inc., 130 Trapelo Road, Belmont, MA, 02478*

Maks J Groom‡ and Qiqi Wang§  
*Massachusetts Institute of Technology, 77 Mass Ave, Cambridge, MA, 02139*

We use numerical solutions to investigate the actuator-disc model in hover. Most solutions come from a conventional Navier-Stokes solver named Flow360, and a few from a Vortex-Ring Method. In Flow360, the source term for vorticity, namely the curl of the force field, is regularized and we have failed to obtain steady solutions with very tight regularizations; the vortex sheet becomes so thin that Kelvin-Helmholtz waves appear, which we consider physically correct. The findings agree with theory and earlier numerical work, and not with the textbook presentations or intuition, and that in three respects. First, even with a uniform pressure jump on a flat disc the velocity through the disc is far from uniform, and it is directed upwards near the rim. The cross-section of the vortex sheet begins as a 45° spiral and therefore it has an initial excursion over the disc, as opposed to a funnel starting downwards with low curvature. Second, again with uniform load, the entire flow field depends only on the rim of the disc, and not on the shape of the surface; only the pressure field reacts to a change in shape (the fluid is incompressible). This opens the door to drooped disc edges/blade tips in actual designs, which could control blade-vortex interaction and also have a "winglet effect" if the rotor diameter is constrained. Third, according to theory, uniform loading gives the lowest power consumption for a given thrust and diameter, in other words the best Figure of Merit, even though the velocity through the disc is so non-uniform; this is because the velocity far downstream is uniform, and that is what controls the power. It is important to invalidate misleading textbook assertions, because astute users will question the results of CFD when they disagree with these assertions. We however find out numerically and from both methods that some non-uniform distributions (higher towards the tip) give a Figure of Merit slightly superior to that from the uniform load; this needs to be explored.

## I. Nomenclature

$R$	=	rotor disc radius
$A$	=	rotor disc area, $\pi R^2$
FoM	=	Figure of Merit, $\frac{T\sqrt{T/2\rho A}}{P}$
$T$	=	rotor thrust
$V_h$	=	induced velocity, $V_h = \sqrt{T/2\rho A}$
$P$	=	rotor power
$\epsilon$	=	actuator disc thickness
$t$	=	dimensional time
$\tau$	=	non-dimensional time, $V_h \cdot t/R$
VRM	=	Vortex-Ring Method
$Re$	=	Reynolds number based on induced velocity and disc radius, $Re = V_h R/\nu$

---

\*Research Scientist, Department of Computational Fluid Dynamics.

†Head of Fluid Mechanics, Department of Computational Fluid Dynamics, AIAA Associate Fellow.

‡Undergraduate Research Assistant, Department of Aeronautics and Astronautics.

§Associate Professor, Department of Aeronautics and Astronautics, AIAA Associate Fellow.

## II. Introduction

Simulations of vertical-flight systems from small to large scales are now routinely conducted even with complex geometries, but it is clear that industrial accuracy is not guaranteed. The reasons range from insufficient grid resolution to inadequate boundary conditions to insufficient time samples, and of course also include simplified physical modeling. A prime example is the use of actuator discs which tend to display an improper response to local flow conditions, and of course ignore the effect of individual blades. As providers of a high-performance CFD system, our company seeks to improve its accuracy in every respect, and a key service is to correctly represent to the customers the accuracy that can be expected depending on the approach. Another service to customers is "design advice," for instance regarding the planform and non-planar aspects of a blade. Some of this is a matter of understanding the real-life flow field, given an efficient enough visualization utility and adequate post-processing effort, but some of it can be addressed through theories of simple problems (such as the pure actuator disc) and by proposing a reasoned "bridge" from pure problems to real geometries (for instance, what can be learned from actuator discs and applied to rotors with actual blades?). In this paper, we describe theoretical-numerical studies devoted to this overall strategy. This is an initial set of studies, which is limited to isolated rotors and therefore fails to address any of the crucial rotor-airframe interactions created by all VTOL aircraft.

A question of long-standing interest is whether a uniform rotor loading is the optimal one, as is asserted by classical actuator-disc theory in many textbooks, and this for all devices from hovering rotors to wind turbines. In the present paper, the new and well-resolved numerical results will confirm that the velocity through the disc is far from uniform and therefore in sharp disagreement with the textbooks, except with very light loading, which implies a rapid climbing condition. This was found by Spalart [1], who rediscovered findings of Schmidt and Sparenberg [2]. The optimality of uniform loading then can appear paradoxical, since the power expended is the product of the pressure jump and the disc-normal velocity, which is now a non-trivial function of radius in accurate flow solutions (being 22% higher in the center than in the average). Reasoning in these terms is very reminiscent of the optimal property of an elliptical span loading for a wing, which produces a uniform downwash, but it is misleading for a rotor that is loaded uniformly all the way to the tip. Such a loading is of course not achievable in practice, but it is a common first approximation in CFD, and is in a way an objective for designs even with a finite number of blades. In any case, the fallacious argument that only uniform "downwash" would explain the optimality of uniform loading is fairly widespread.

The opposing argument to the uniform-velocity reasoning is as follows. It considers it possible that the velocity distributions across the disc will result in exact cancellations, so that the simple theoretical results are not affected [1], and it focuses on the stream tube far downstream. In a control-volume analysis, this tube contains a flux of momentum, which equals the thrust, and a flux of kinetic energy, which equals the power. The fluid originates at infinity, with a sink-flow behavior and a velocity of order  $1/r^2$  for large  $r$  (here in spherical coordinates). Therefore, the integrals over a large sphere of any power of the velocity equal to or larger than 2 tends to zero. Both fluxes inside the wake are the integral versus  $r$  of powers of the axial velocity, represented by  $V_y(r)$  in this paper, at a radius  $r$  from the axis ( $r$  now in cylindrical coordinates). Minimizing the latter quantity (power) while fixing the former (thrust) allows a simple proof via a Lagrange multiplier of the fact that uniform far-field velocity is indeed optimal. It then demands a uniform pressure loading.

Figure 1 illustrates the major flow features we are exploring here. A numerical solution from a spectral method by Spalart [1] for an actuator disc with uniform loading clearly displays the vortex sheet initially propagating upwards, and then diving through the disc. The (dashed) velocity contours on the left side confirm the upwards velocity within part of the disc and outside it. The figure also shows in gold a possible non-planar shape for the rotor, that is the surface on which the pressure jump is imposed. which is taken up below.

In recent work by Bontempo and Manna [3], the distribution for maximum power by a wind turbine, which is a related problem, is calculated with a Euler-Lagrange equation, and it was found that the maximality condition there also requires  $V_y$  to be independent of  $r$ . Since  $V_y(r)$  far downstream on a streamline is a function of the local loading  $\Delta p(r)$  where the streamline crosses the disc through Bernoulli's equation, this shows that  $\Delta p$  must be independent of  $r$ . All the streamlines inside the streamtube have crossed the disc once, and therefore received a step in total pressure equal to  $\Delta p$ . The findings of Bontempo and Manna are not fully identical to ours, however, because they invoked an approximate one-dimensional form of the momentum equation, and correctly concluded that their proof was therefore not quite complete. In their reasoning, it left the door open for the Betz maximum power coefficient of 16/27 not to be the true maximum. The Lagrange-multiplier proof shows that their approximation is not needed, and therefore their result is more rigorous than they thought.

Accurate numerical solutions will establish the velocity through the disc and far downstream, as well as the streamtube shape, for which we do not know of an analytical solution. They will confirm or falsify the relationship

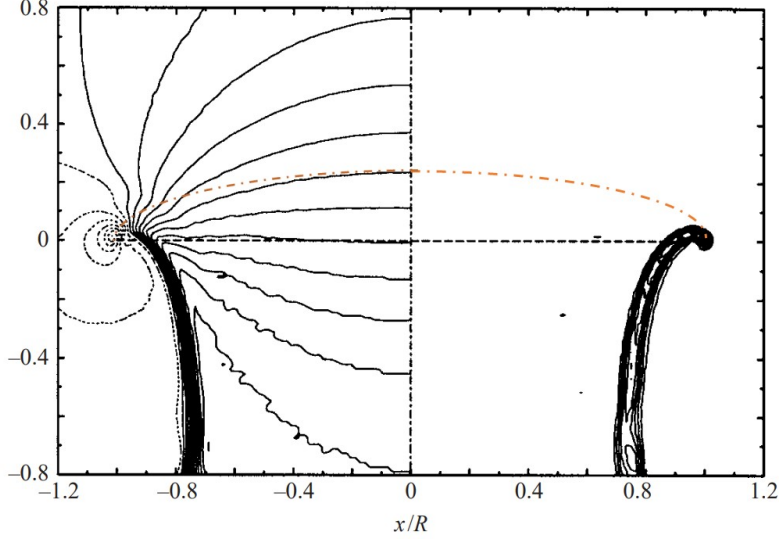


**Fig. 1** Flow field near actuator disk in hover,  $U_\infty = 0$ . Laminar solution with spectral method (2003). Left, contours of axial velocity; —: down, - - -: up. Right, contours of vorticity [1]. Gold, possible alternate shape of the actuator surface.

between  $V_y$  and  $\Delta p$  on a streamline, as well as the two ways to calculate either the thrust or the power, which should be equivalent. They will also test the property that the vortex sheet leaves the rim of the disc with for its cross-section a 45 deg spiral. Spalart observed indications of this, but did not have a very fine grid, so that the vortex sheet was fairly thick in Figure 1. The present study will investigate the optimal distribution of disc loading numerically using both the viscous actuator disc method [4] and the inviscid vortex-ring method [5]. In the viscous actuator disc solver, the Navier-Stokes equations are solved. To avoid smearing the vortex tube in the far downstream to a developed turbulent jet, no turbulence model is turned on. Compared to the classical actuator disc theory, where the flow is assumed to be incompressible, inviscid and isentropic, the viscous compressible flow in the Navier-Stokes solver may mess up the conclusion. We still use the viscous Navier-Stokes solver in the present study because all rotors work in viscous flow in practice. Also, Figure 1 had no turbulence model too and it had the regularization of the source term and viscosity; nevertheless the flow field shows that the state of an essentially straight vortex tube is reached over a distance sufficient to expect close agreement between Navier-Stokes and inviscid theory for the principal quantities of interest (thrust and power). To assess the impact of viscosity and compressibility, firstly, a comparison on flow solutions in various Reynolds numbers and induced velocity is conducted.

Secondly, in pure theory, the actuator disc method models the rotor effects via a disc with infinitesimal thickness, which introduces a pressure jump in the direction normal to the actuator surface to model the thrust, and a tangential velocity to mimic the torque, in more elaborate versions (this is left for future work). However, in Navier-Stokes simulations, the thickness of actuator disc has to be a finite value, and in addition  $\Delta p$  does not fall to 0 vertically at the disc's edge. Interacting with this regularization in two directions, the grid resolution near the disc can impact the flow solution, and to capture this we will first test three different grid resolution levels and three actuator-disc regularization levels respectively.

Thirdly, we will verify that, with uniform disc loading, the flow field depends only on the disc rim, and not on the shape of the surface [2]. The source term for the azimuthal vorticity  $\omega_\theta$ , which is the curl of the body force, is  $\Delta p / \rho \delta(r - R, 0)$  where  $\delta$  is the Dirac distribution; integrated, it increases the impulse  $J_y$  in time at the rate  $T / \rho$ , during the transient before the perturbations approach the boundaries of the numerical domain. This independence property is very relevant to non-planar actuator surfaces, for instance with "droop" or "winglets," creating a degree of freedom which is part of our "design advice." Since any non-planar surfaces could be approximated by distributions of simple flat, conical or cylindrical ones, to make things simpler, three different actuator surfaces with cross-sections made of straight segments, denoted by flat, cone and cap, are investigated in the present study, as shown in Figure 2. Furthermore, as is well known, uniform loading gives zero vorticity in the streamtube, and if approximating a real rotor with blades, it would require there to be no trailing vorticity, and therefore that the blade circulation  $\Gamma(r)$  be constant. This can be

achieved with a constant lift coefficient  $C_l(r)$  and a chord distribution inversely proportional to  $r$ :  $c(r) \propto 1/r$ . This is visually consistent with wind-turbine designs except approaching the tip, but not at all with helicopter designs; some of the drone rotors have this character at least in terms of concave  $c(r)$  distributions. However, the quantity that needs to be constant is actually  $rc(r)C_l(r)$  where  $C_l$  is the lift coefficient, and this can be achieved with blade twist. All of these arguments overlook the blade tip loss effects, which brings up the aforementioned "bridge" between the simplest models and actual designs. Specifically, to explore the blade tip effects at low cost and in a steady state, we split the actuator disc into 2 parts: an inboard portion  $r/R \in [0, 0.7]$  with pressure jump  $\Delta p_{in}$  and an outboard portion  $r/R \in [0.7, 1]$  with pressure jump  $\Delta p_{out}$ . Under the same amount of total thrust, by varying the ratio of  $\Delta p_{out}/\Delta p_{in}$ , the flow fields are compared and the impact on rotor efficiency is calculated.

The paper proceeds with sections on Methodology, on Results and Discussion, and a set of Conclusions and Future Plans.

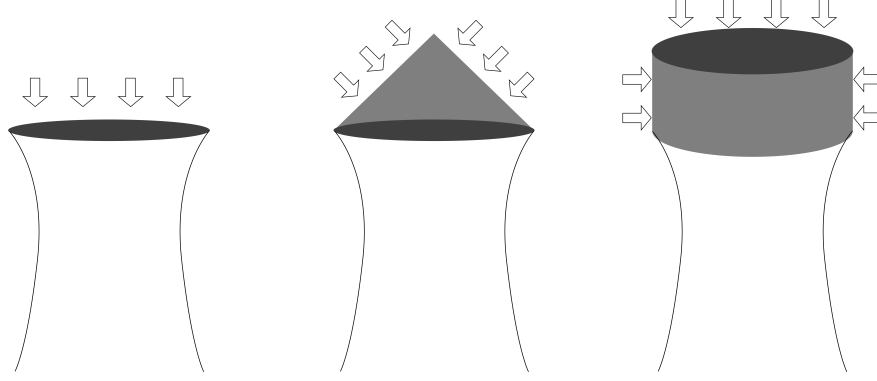


**Fig. 2 Three different shapes of actuator surfaces: flat (left), cone (middle) and (cylindrical) cap (right). Arrows show the imposed loading.**

### III. Methodology

Two CFD methods are used in the present study to investigate the hovering actuator disc: viscous actuator disc formulation in Navier-Stokes and inviscid vortex-ring method.

#### A. Viscous Approach Using Actuator Disc Formulation

The viscous actuator disc model is realized by adding a source term of momentum inside the cylindrical disc region in the Navier-Stokes equations as a pressure jump across the surface. Because of the axisymmetric nature of the flow, to reduce the total computational cost, we performed CFD simulations in a 2-degree sector domain shown in Fig. 3. The center of the sector is the axis of the actuator disc. To avoid the mesh singularity at the axis, we terminated the computational domain at an inner radius of 1% of the actuator disc radius, denoted by  $R$ . The outer radius of the domain is  $5R$ . The height of the sector is  $10R$ , with the actuator disc placed at the center. 5 layers of grid points are spaced uniformly in the circumferential direction. The farfield mesh is shown in Fig. 4. The reason of using such a compact domain ( $5R \times 10R$ ) is that, in a bigger domain, e.g.  $10R \times 20R$ , there would be an upwash region led by a vortex, which dramatically ruin the entire flow pattern and lead to Figure of Merit  $> 1$ . To overcome this issue, besides a  $5R \times 10R$  domain is used, an energetic boundary condition with weakly imposed velocity field was used on farfield boundaries. The velocity field on farfield boundaries came from a modified farfield flow model in [6], which was originally proposed in [7].

Three different shapes of actuator discs are considered: flat, cone and cap. For each shape, 3 meshes with coarse, medium and fine resolution in and near the disc region are generated, which are shown in Figure 5. The edge length in the disc region and the number of grid points are listed in Table 1.

The parameters in the simulations are shown in Table 2: 3 different disc thickness, 4 different disc loading, 3 different Reynolds numbers are covered in the present study. In the investigation of the influence of varying distribution of disc loading at the same amount of total thrust, the ratio of outboard loading over inboard loading,  $\Delta p_{out}/\Delta p_{in}$ , ranges between 0.2 and 5. For a given total thrust and  $\Delta p_{out}/\Delta p_{in}$ , it is easy to calculate the  $\Delta p_{out}$  and  $\Delta p_{in}$  respectively via

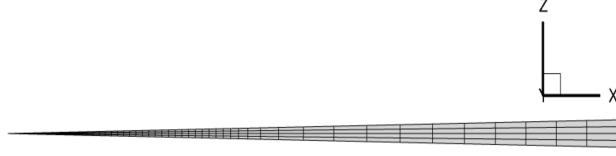


**Fig. 3** The quasi-two-dimensional sector domain created by extruding  $2^\circ$  in the circumferential direction

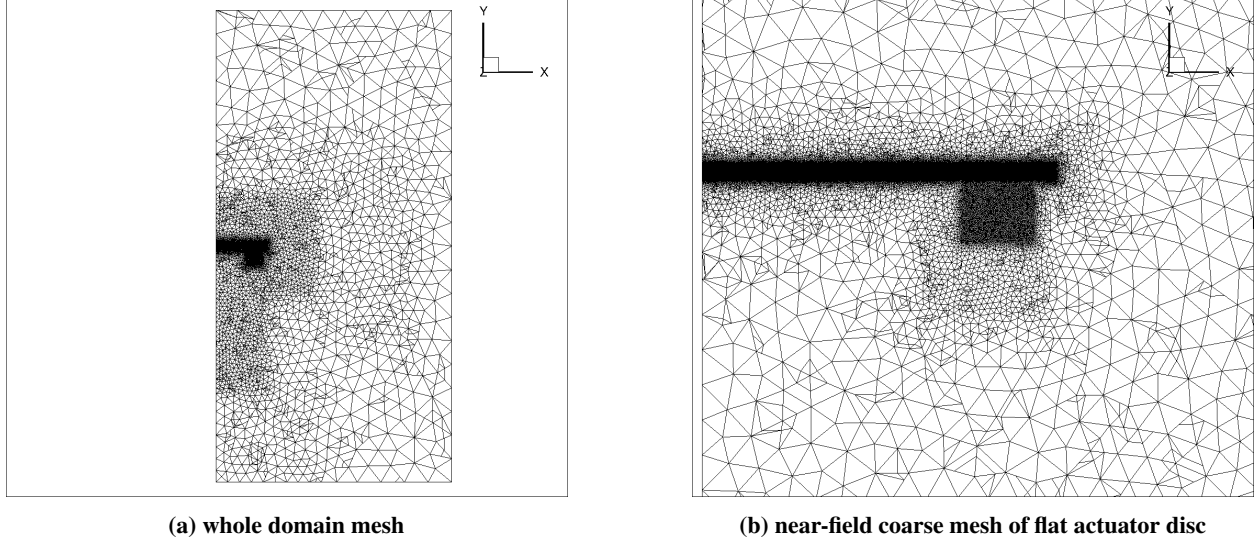


**Fig. 4** Overview of the farfield mesh.

**Table 1** Grid resolution

mesh parameter	coarse	medium	fine
edge length within disc, $\Delta s/R$	0.1%	0.05%	0.025%
number of grid point in mesh (flat)*	360K	954K	5.47M
number of grid point in mesh (cone)*	552K	2.00M	7.60M
number of grid point in mesh (cap)*	589K	2.11M	8.08M

\* The number of grid point contained by the domain of  $2^\circ$  sector.

Equation 1. As customary, we use the Figure of Merit to represent the efficiency, defined in Equation 2. It should be noted that the total thrust and  $V_h$  are one-to-one matched via the formulation  $V_h = \sqrt{T/2\rho A}$  based on the classical momentum theory, so we will use  $V_h$  to represent the total thrust (or pressure jump) in following sections. Besides, since there is a shear layer across the streamtube, where Kelvin-Helmholtz instability may develop if the viscosity fails to dampen the perturbations, so the flow could be unsteady (e.g. Figure 7a). Therefore, all simulations related to the viscous actuator disc approach were started from a steady-state solution as initial condition and then restarted using the 2nd-order time-accurate unsteady solver in Flow360. Besides, because multiple thrust levels, thus different  $V_h$ , are involved in the viscous actuator disc simulations, a non-dimensional time  $\tau \equiv V_h \cdot t/R$  is used to scale any physics in time.

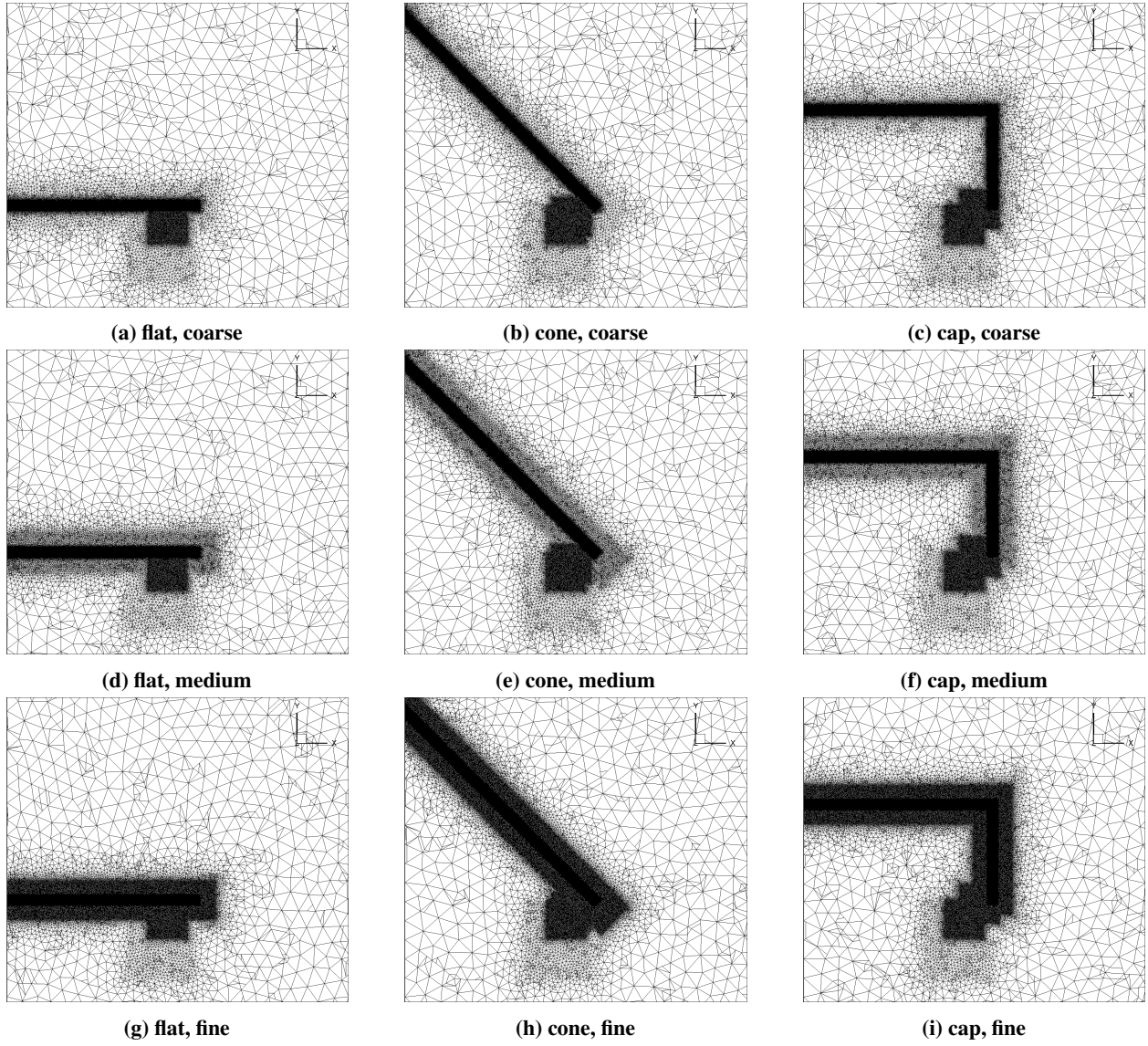


**Fig. 5** Zoomed-in view of the near-field region of coarse, mesh and fine meshes containing 3 different shapes of actuator surface: flat, cone and cap

**Table 2 Simulation parameters of the viscous approach using actuator disc formulation**

parameter	value(s)
disc thickness, $\epsilon$	$1\%R, 2\%R, 4\%R$
induced velocity, $V_h^*/C_\infty$	0.05, 0.025, 0.0125, 0.00625
Reynolds number $Re_i(V_h^*, R)$	$1e3, 4e3, 1e4$
$\Delta p_{out}/\Delta p_{in}$	$0.2 \sim 5$

\* induced velocity in hover,  $V_h = \sqrt{T/2\rho A}$

$$\begin{aligned}
 T &= \int_0^R \Delta p(r) 2\pi r dr \\
 &= \int_0^{0.7R} \Delta p_{in} 2\pi r dr + \int_{0.7R}^R \Delta p_{out} 2\pi r dr \\
 &= \pi R^2 \Delta p_{in} (0.49 + 0.51 \Delta p_{out}/\Delta p_{in})
 \end{aligned} \tag{1}$$

where

$\Delta p_{in}$  : constant static pressure jump in the inboard portion  $r/R \in [0, 0.7]$

$\Delta p_{out}$  : constant static pressure jump in the outboard portion  $r/R \in (0.7, 1]$

$$\text{Figure of Merit} = \frac{T \sqrt{T/(2\rho A)}}{P} \tag{2}$$

where

$T$ : total thrust of the full actuator disc, which is an input in present study.

$P$ : total power of the full actuator disc, which is calculated by  $P = \iiint_{V_{AD}} \vec{f} \cdot \vec{V} dV$ , where  $\vec{f}$  is the imposed body force per volume,  $\vec{V}$  is the velocity vector, and  $V_{AD}$  is the volume where the momentum source term is imposed in the actuator disc formulation.

## B. Inviscid Vortex Ring Approach

The actuator disc was also simulated with an inviscid vortex method, based on discretizing the steady wake vortex sheet with axisymmetric vortex rings. Our formulation is adapted from that of Bontempo and Manna (2018) [5] to treat rotors in hover and with non-uniform loadings.

In the case of a uniform loading, the actuator disc generates a wake only at the rim. The strengths and positions of the vortex rings representing the wake are obtained by iteratively enforcing two sets of constraints, namely that the wake is a streamsurface of the flow, and that it does not sustain a static pressure jump. From the first constraint, we require that the tangent vector of the wake sheet is aligned with the local flow velocity induced at each ring. From the second constraint,  $p_{t,out} - \frac{1}{2}\rho u_{out}^2 = p_{t,in} - \frac{1}{2}\rho u_{in}^2$ , where  $p_{t,out}$  and  $u_{out}$  are the total pressure and velocity just outside the vortex sheet, while  $p_{t,in}$  and  $u_{in}$  are the total pressure and velocity just inside the vortex sheet. We can therefore obtain a relation for the vortex sheet strength  $\gamma$  from the total-pressure jump on the disc  $\Delta p$  and the local velocity:

$$\begin{aligned}
 \Delta p &= p_{t,in} - p_{t,out} \\
 \gamma &= u_{out} - u_{in} \\
 u_{sheet} &= (u_{out} + u_{in})/2 \\
 \gamma &= -\Delta p/(\rho u_{sheet}).
 \end{aligned} \tag{3}$$

The wake consists of linear panels with a vortex ring element at a collocation point at the midpoint. The vortex rings are regularized [8] with a small fixed core width to prevent instability, and to allow evaluation of the self influences. The self terms are therefore evaluated directly rather than with the more complicated curvature scheme of [5]. The circulation on each ring is  $\gamma s$ , where  $\gamma$  is the local sheet strength, and  $s$  is the length of the wake segment. The free portion of the

wake extends for 5 diameters downstream of the disc, and is discretized with a cosine spacing to concentrate refinement near the high curvature region close to the disc. To approximate the streamtube behavior far downstream, a cylindrical vortex element of constant radius discretized with a constant spacing of vortex rings is appended to the free wake and extends for an additional 5 diameters downstream.

The free wake elements and cylindrical wake element are initialized to the radius of the disc, with the circulation based on the asymptotic sheet strength, which is  $\gamma_\infty = \sqrt{2\Delta p/\rho}$  [1] at downstream infinity. In each iteration, the velocity induced by the wake is computed at the first element. The strength is updated according to (3), while the position is updated by computing the displacement vector of the end point to realign the panel with the local flow, and then shifting the end point and all downstream points by the displacement vector scaled by a relaxation parameter  $\beta$ . The same procedure is then performed sequentially at each downstream panel. Convergence is measured with a residual, defined as the sum of the magnitudes of the normal velocities at each panel at the end of the iteration, weighted by the length of each panel.

To model discs with non-uniform loadings, multiple discs with different radii are superimposed. The iteration procedure for each disc wake is performed sequentially, and the residual to be converged is taken as the maximum of each wake residual. This allows simulation of discs with general piecewise-constant loadings, with a separate wake sheet at each discontinuity in the pressure jump. The method may face convergence issues if the wakes are placed very close together compared to the wake refinement, or if the free wakes intersect or cross as they evolve from their initial position to their equilibrium position.

The thrust and Figure of Merit are computed as in equations (1) and (2). The power is obtained by integrating the product of the normal velocity and the pressure jump over the actuator surface:

$$P = \int_0^R \Delta p(r) u_z(r) 2\pi r dr \quad (4)$$

This integral is evaluated numerically with the trapezoidal rule with 20000 points.

## IV. Results and Discussion

This section shows the results of numerical investigation of the flow over a hovering rotor using the viscous actuator disc approach and the inviscid vortex-ring method. We will first get a set of proper parameters in the viscous approach, e.g. mesh resolution, surface shape,  $Re \equiv V_h R/\nu$ , thrust (setting  $V_h$ ) and regularization level ( $\epsilon$ ), through a series of assessment in sections IV.A to IV.C. After that, a detailed comparison between the two approaches under both uniform and non-uniform disc loading is conducted in section IV.D.

### A. Viscous actuator disc approach in different $Re$ and $V_h$

Firstly, the impact of viscosity and compressibility in the viscous actuator disc approach are investigated. Three different Reynolds numbers  $Re = 1e3, 4e3, 1e4$  and two different levels of induced velocity (or thrust or pressure jump) are simulated using flat actuator surface on coarse mesh. Figure 6a shows the convergence of the nonlinear residual on the mass, momentum and energy. Figure 6b shows their FoM. It can be seen that all FoM fall in  $[0.979, 1.005]$ . For the high Reynolds number  $Re = 1e4$ , the residuals hang around  $10^{-8}$  for both induced velocities and the FoM show evident oscillations. For the medium and low Reynolds number:  $Re = 1e3$  and  $Re = 4e3$ , residuals could be converged under  $10^{-11}$  and their FoM become flat over time marching. It indicates the flow under  $Re = 1e4$  becomes unsteady. The z-component of instantaneous vorticity of  $Re = 1e4$ ,  $V_h/C_\infty = 0.05$  and  $Re = 4e3$  and  $1e3$ ,  $V_h/C_\infty = 0.025$ , shown in Figure 7, verifies the observed phenomena. For the high Reynolds number  $Re = 1e4$ , the Kelvin-Helmholtz instability was triggered. The peak vorticity is higher, as expected. This simulation will not produce true turbulence because it lacks the third dimension. The  $Re = 1e3$  smears the tip vortex (stream spiral) evidently. Therefore, to reduce the impact of viscosity and compressibility as well as resolve the stream spiral better, we choose the medium Reynolds number  $Re = 4e3$  and  $V_h = 0.025$  in the following Section IV.B and Section IV.C.

Qualitative comments are in order about the Kelvin-Helmholtz instability. There is no proof that this instability will not develop, particularly if the vortex sheet is made very thin, and therefore make the steady-state solver fail. Figure 1, from a very different numerical method, shows mild waviness in the vorticity contours very similar to Figure 7a. This depends on how much the pressure jump is regularized, and on the Reynolds number based on  $R$  or  $\epsilon$ . This flow has a receptivity mechanism at the rim of the disk where vorticity is injected, hinging on a pressure feedback from the sheet to that vorticity source which is fixed in space not unlike a solid surface. In other words it has similarities with



the mechanism at the trailing edge of a jet nozzle, but is far from identical to it. In both cases, the thin shear layer is convectively unstable; it may also be absolutely unstable for linear perturbations, and as a result grow in time until it reaches a finite-amplitude nonlinear limit cycle.

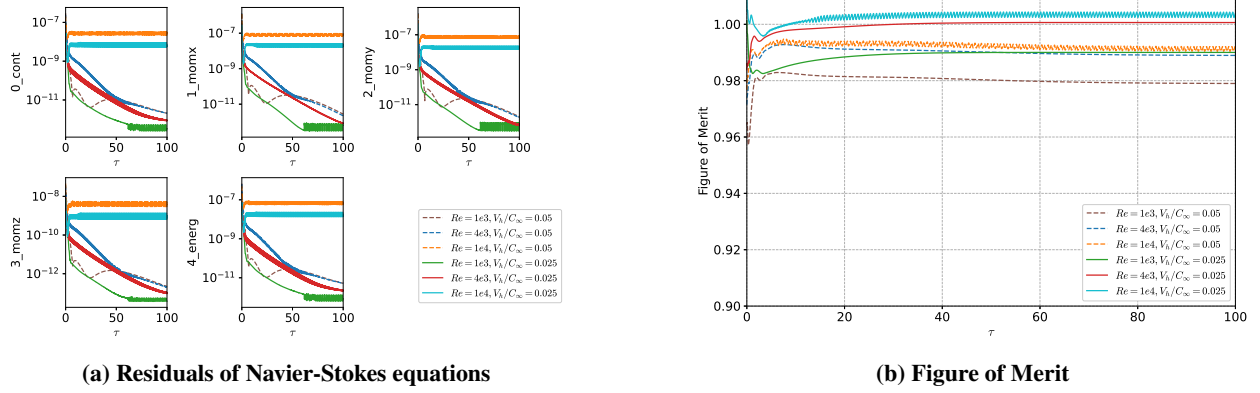


**Fig. 6** Convergence of residual and Figure of Merit of viscous Actuator Disc simulations for different Reynolds numbers and pressure jumps.

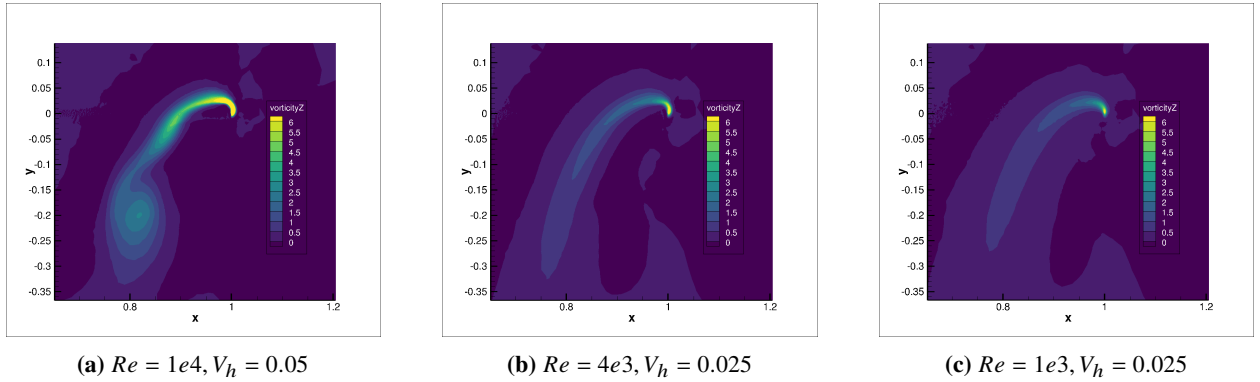


**Fig. 7** Vorticity of flow by viscous actuator disc approach obtained on flat surface, coarse mesh,  $\epsilon = 2\%R$ : (a)  $Re = 1e4, V_h = 0.05$  (b)  $Re = 4e3, V_h = 0.025$  (c)  $Re = 1e3, V_h = 0.025$

### B. Viscous actuator disc with different mesh resolution and disc thickness $\epsilon$

For the viscous actuator disc with flat surface with uniform loading, the convergence history of FoM based on instantaneous flow on coarse, medium and fine meshes and  $\epsilon = 1\%R, 2\%R, 4\%R$  is displayed in Figure 8a. Since evident unsteadiness is shown, especially for medium and fine meshes, to illustrate the averaged performance and flow features, the time-averaged FoM and contour of Mach number is shown in Figure 8b and Figure 9 respectively. It can be seen that the mesh resolution and disc thickness don't visibly change the flow and FoM. The difference brought by the grid resolution inside the disc region is smaller than 0.5% for each regularization level. The relative difference in FoM is smaller than 1% in all situations. The convergence history of FoM on cone and cap surface shapes shows the similar behavior, so they are omitted here. In the following sections, the coarse mesh with  $\epsilon = 2\%R$  will be used by default.

### C. Viscous actuator disc with 3 surface shapes: flat, cone and cap

The three actuator surface shapes were simulated on the coarse meshes with  $\epsilon = 2\%R$  and uniform disc loading  $V_h/C_\infty = 0.025$  respectively. For every each surface shape, the contours of pressure,  $z$ -vorticity,  $y$ -velocity and  $x$ -velocity are shown in Figure 10. It can be seen that although different surface shapes have dramatically different pressure distributions, the velocity field is almost identical due to having the same vorticity, which verifies that the flow

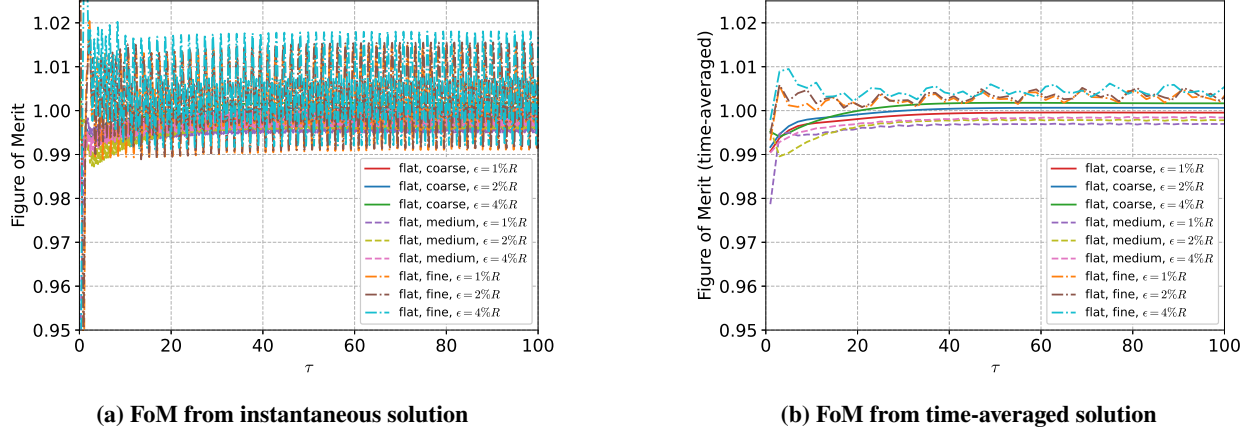


**Fig. 8** Figure of Merit by viscous actuator disc approach on flat actuator surface with uniform loading with different mesh resolutions and regularization levels based on (a) instantaneous (b) time-averaged solutions. ( $Re = 4e3$ ,  $V_h = 0.025$ )

field only depends on the rim of the disc if the pressure jump is uniform. The convergence history of Figure of Merit is shown in Figure 11. It can be seen that the relative difference of FoM between 3 surface shapes is within 1%. Therefore, the flat surface will be used in following sections. For real rotors, it means the tip region of the blades has a big influence on the induced velocity field encountered by the following blade, and so the design of the wing tip and blade tip can be guided by CFD. For example, Archer’s Maker, a recently introduced production eVTOL aircraft now in early flight test, uses drooped blade tips presumably to enhance the performance by managing the blade-vortex interaction [9].

#### D. Comparison between viscous actuator disc approach and inviscid vortex-ring method (VRM)

A comparison between the viscous actuator disc approach and the inviscid vortex-ring method with uniform and non-uniform disc loading is shown in this subsection. The viscous approach ran on the coarse mesh with the flat actuator surface,  $\epsilon = 2\%R$ ,  $Re = 4e3$ , which was verified in previous sections. The inviscid vortex method was applied to a uniform disc case of unit radius  $R$  and unit pressure jump  $\Delta p$ . The ring core size was fixed at  $\sigma/R = 0.00001$ , with 300 elements in the free wake and 200 elements in the far wake cylinder. For uniform disc loading, the convergence plot for the Figure of Merit of the uniform disc is shown in Figure 12a. It has a Figure of Merit of 1.0076 and an average axial velocity on the disc of  $V_h = 0.7018$ , which compare well with the theoretical values of  $FoM = 1$  and  $V_h = \sqrt{0.5} \approx 0.7071$ . Figure 12b shows the detail of the wake development around the disc edge using VRM, which closely matches the theoretical log spiral as it approaches the rim [1]; we believe this is the first example of such a conclusive agreement. The plot shows a notable upward velocity at the tip until about  $r/R = 0.88$ , in good agreement with Fig. 1. The crossing of the flat disc and the vortex sheet near  $r/R = 0.88$  could be interpreted as a “very simple form of Blade-Vortex Interaction” and suggest curving down the blade tip to raise the blade itself above the vortex sheet. This is physically consistent, but not quantitatively in practice. The point is that with actual blades the tip vortex starts inboard of the rim, because the blade’s circulation drops to 0 over some distance, and also the bound vortex of the blade first deflects the tip vortex downward; it is then deflected upwards by the vortices from the preceding blades, which are inboard of it. Therefore, well-resolved CFD will be necessary to manage BVI.

The streamlines of both the viscous actuator disc approach and the inviscid vortex-ring method under uniform disc loading are shown side-by-side in Figure 13 at two zoom levels. The far-field streamlines in the second graph are quite different. This is due to the far-field boundary condition derived for a turbulent wake, which has streamlines directed downwards everywhere. In contrast, the VRM has an inviscid wake, and its far-field is that of a sink flow, with streamlines directed towards the origin. The streamlines near the disk itself are in much better agreement, being dominated by the vortex sheet. One also notices how the Navier-Stokes shear layer is thickened by viscosity, whereas that of the inviscid method is still very thin, with an abrupt change of direction around  $r = R/\sqrt{2}$ ; this is confirmed by curves in a later figure.

In Figure 14, the VRM’s rim streamline (red curve) is plotted on top of the streamlines and Y-component velocity field of the viscous actuator disc approach. For simplicity, the flow solution of flat shape Actuator Disc with fine mesh

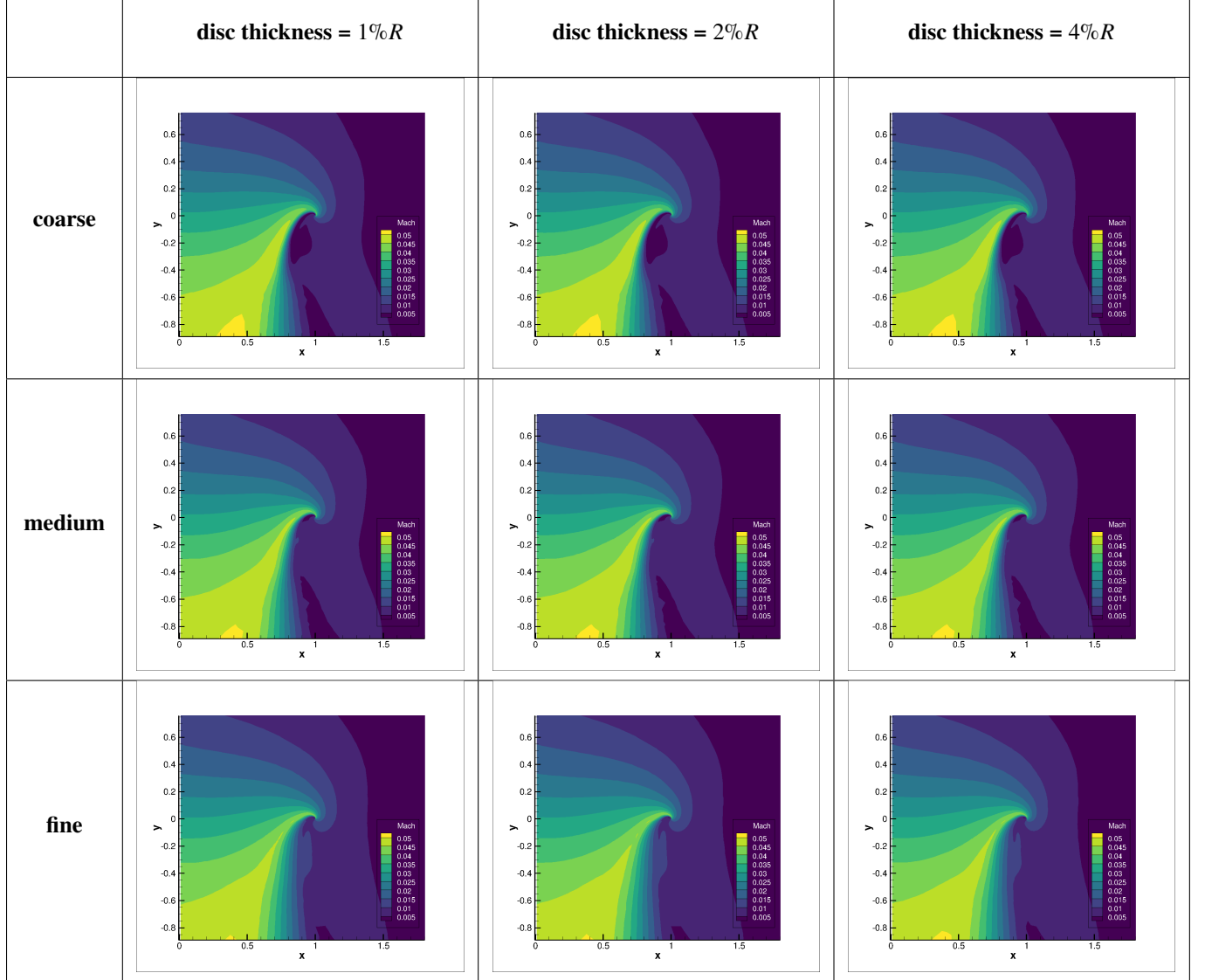


**Fig. 9** Time-averaged Mach number of flat actuator surface with uniform loading  $V_h/C_\infty = 0.025$ .

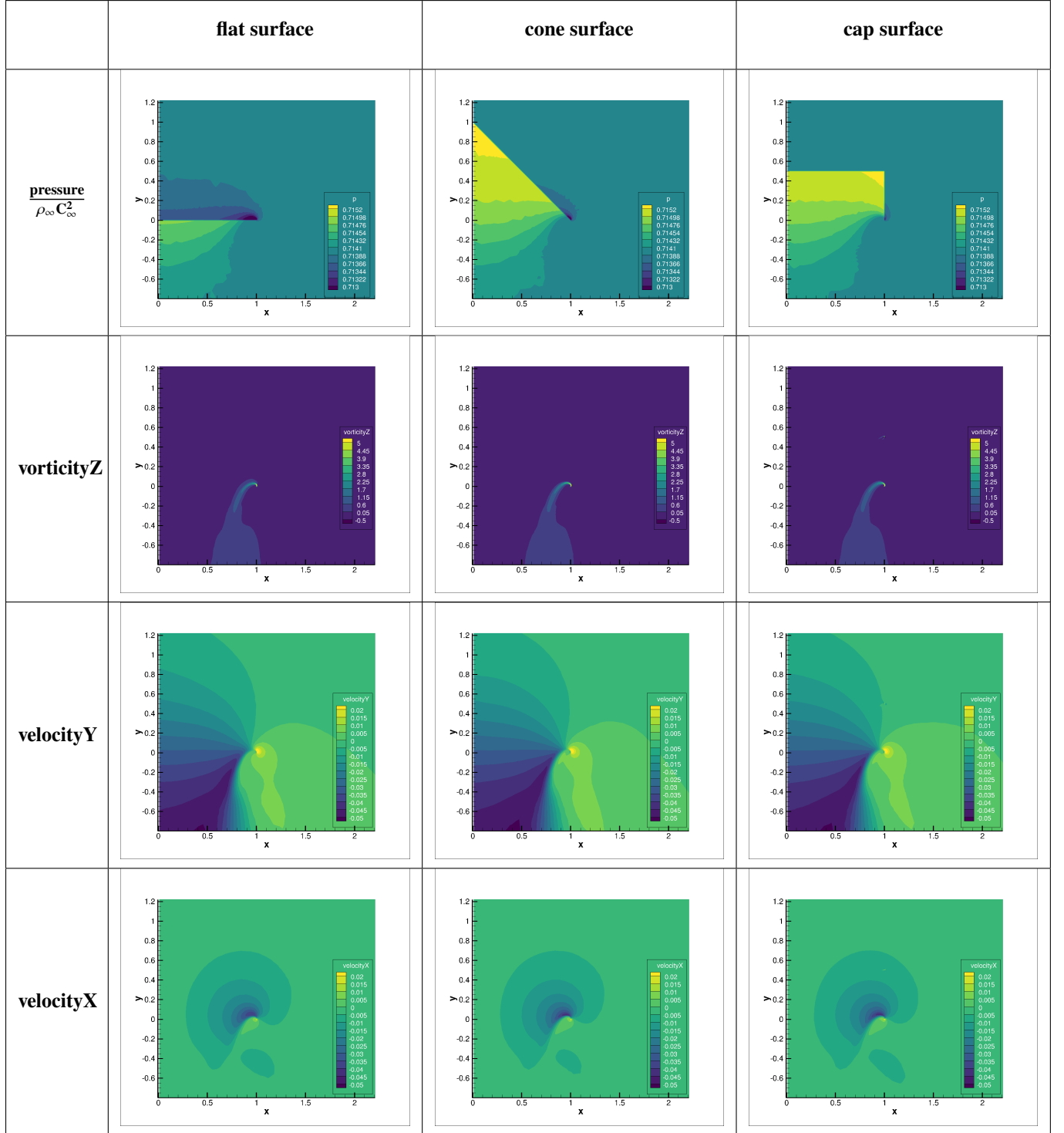


**Fig. 10** Flow field comparison between 3 shapes of actuator disc on coarse mesh with  $\epsilon = 2\%R$  under uniform disc loading  $V_h/C_{\infty} = 0.025$ .

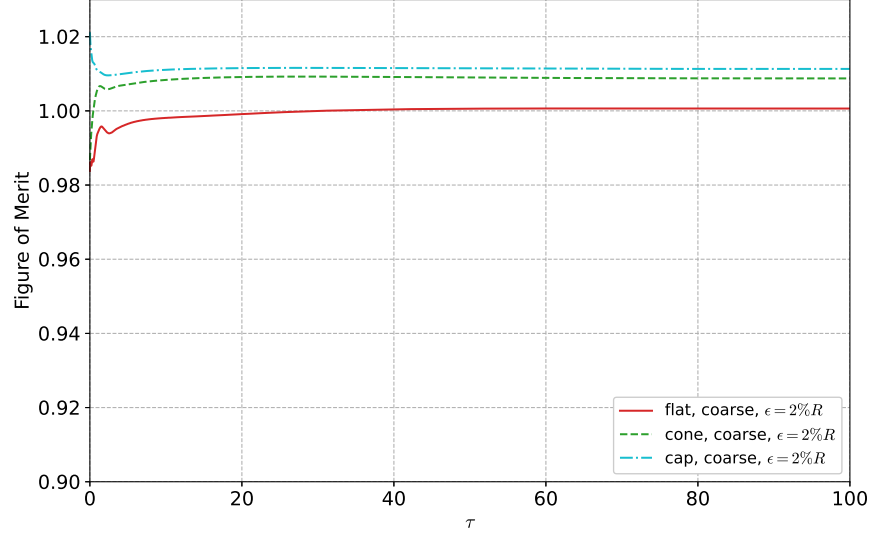
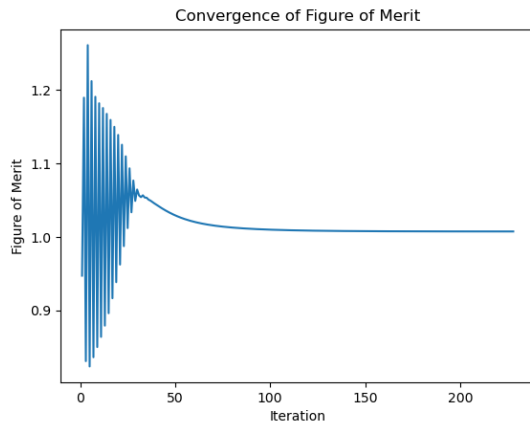
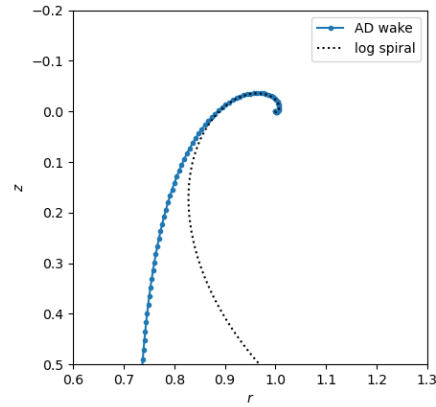


**Fig. 11** Figure of Merit of flat, cone and cap actuator surfaces with  $2\%R$  thickness and  $V_h/C_\infty = 0.025$  in coarse meshes.

and disc thickness  $\epsilon = 2\%R$  is chosen to represent the Actuator Disc method. It can be seen that the streamlines of both methods agree well with each other in the down-wash region. Near the rim of the disc, the streamline of the VRM agrees well with the analytical expression  $r(\theta) = e^{\theta + 0.3041\pi}$ , where  $(r, \theta)$  are now polar coordinates centered at  $(1, 0)$ , as denoted by the cyan curve (the spiral solution is two-dimensional and can be rotated arbitrarily). The viscous streamlines are affected by the regularization very near the  $(1, 0)$  point, but they rapidly start following the spiral. A finer comparison of the radial and axial velocity components on the disc of both viscous actuator disc approach and inviscid VRM is shown in Figure 18, normalized by the induced velocity. The viscous solution smooths out the jumps, but it is apparent why the integral of  $V_y$ , which sets the crucial FoM, is very close between the two fields. The known fact that  $V_y$  is below  $-V_h$  over most of the disc ( $[0, \sim 0.88R]$ ) and then becomes positive ( $r = 0.92R$  for viscous approach due to viscosity) is also evident.



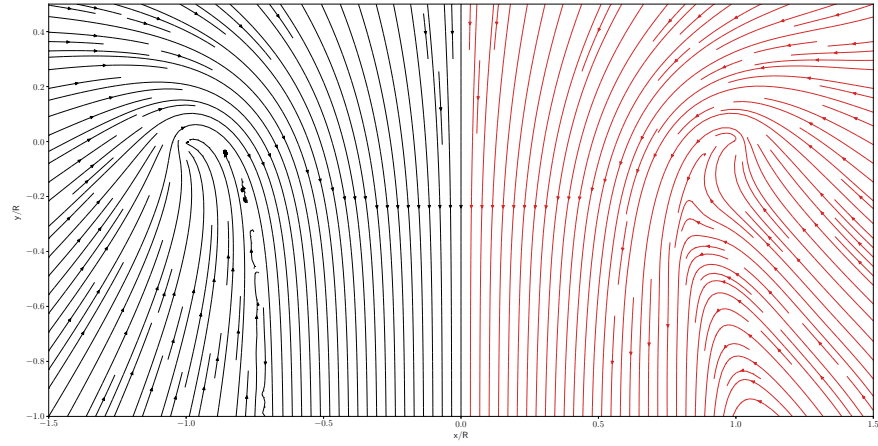
(a) FoM from instantaneous solution



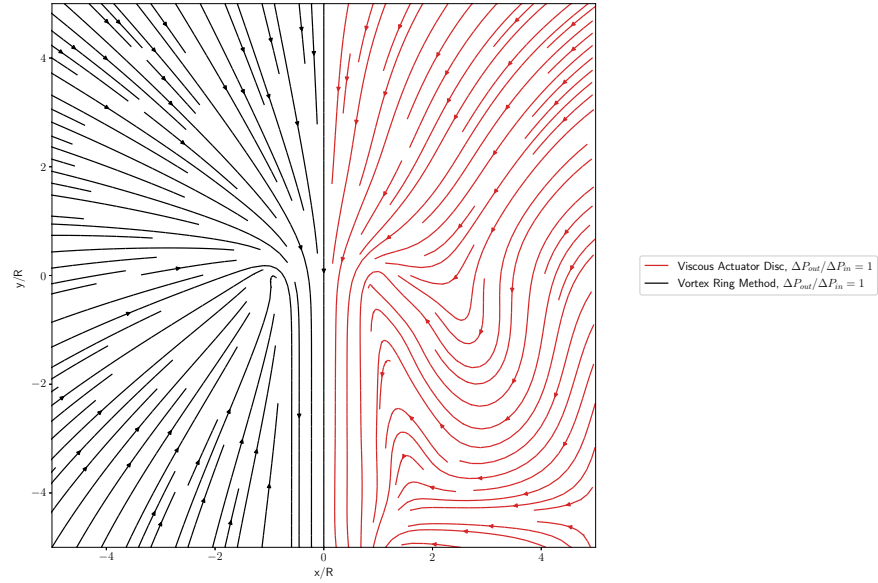
(b) Wake development around the disc edge in uniform loading and a log spiral

**Fig. 12** Simulations of uniform loading disc by the vortex-ring method.

To study effects similar to those of blade tips at a low computational cost, as stated in section III, the disc is split into an outboard and an inboard portion at the radial location  $r = 0.7R$ . Multiple CFD simulations were conducted by



(a) zoom-in view



(b) zoom-out view

**Fig. 13** Streamlines obtained by viscous actuator disc approach (flat surface, coarse mesh,  $\epsilon = 2\%R$ ,  $V_h/C_\infty = 0.025$ ,  $Re = 4e3$ ) and inviscid vortex ring approach with uniform loading  $\Delta p_{out}/\Delta p_{in} = 1$  in (a) zoom-in and (b) zoom-out views.

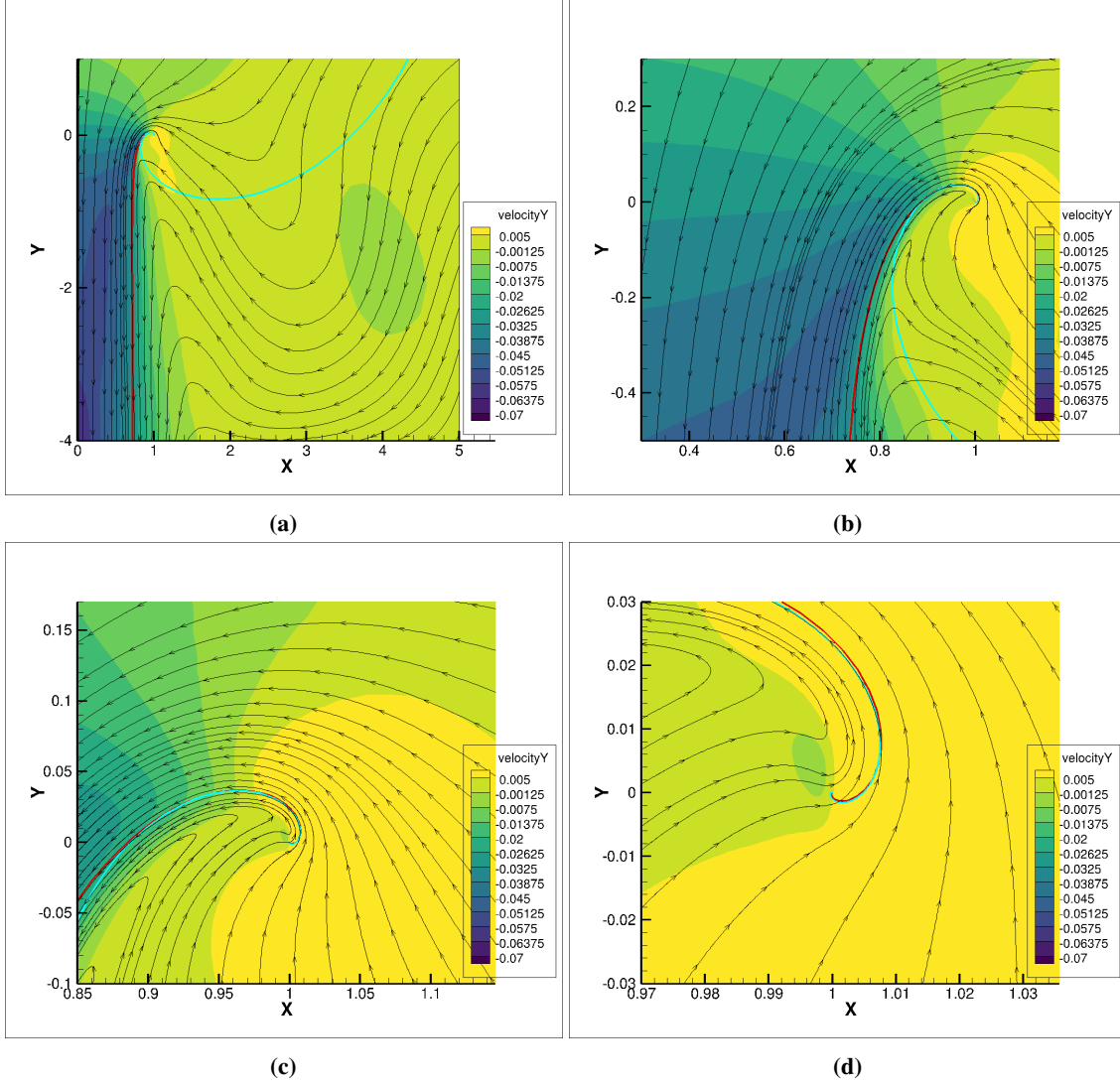


**Fig. 14** Streamlines of flow in uniform disc loading,  $\Delta p_{out}/\Delta p_{in} = 1$ , solved by Viscous Actuator Disc approach (arrowed black lines, with flat surface, coarse mesh,  $\epsilon = 2\%R$ ,  $Re = 4e3$ ,  $V_h/C_\infty = 0.025$ ) and inviscid Vortex Ring Approach (red line) in finer and finer zoom levels from (a) to (d). The cyan curve represents a spiral curve:  $r(\theta) = e^{\theta+0.3041\pi}$ . Contour of Y-component of velocity resulting from viscous Actuator Disc Method.

varying the  $\Delta p_{\text{out}}/\Delta p_{\text{in}}$  between 0.2 and 5 for the flat actuator surface on the coarse mesh with  $\epsilon = 2\%R$  under different total thrust. The convergence history of Figure of Merit of varying  $\Delta p_{\text{out}}/\Delta p_{\text{in}}$  is shown in Figure 15. The resulting pressure and velocity field with the same total thrust  $V_h/C_\infty = 0.025$  but different loading distribution using the viscous actuator disc approach is shown in Figure 16. The inviscid vortex ring method was also applied to piecewise-constant non-uniform disc loadings, with an inner pressure jump  $\Delta p_{\text{in}}$  specified on the disc from  $r/R = [0, 0.7]$  and an outer pressure jump  $\Delta p_{\text{out}}$  specified on the disc from  $r/R = (0.7, 1]$ . Figure 17 shows the Figure of Merit over a range of  $\Delta p_{\text{out}}/\Delta p_{\text{in}}$  loading ratios, showing the optimal efficiency of VRM at  $\Delta p_{\text{out}}/\Delta p_{\text{in}} = 4/3$  that exceeds the performance of the uniform loading by about 1%. This is a very small difference. It also shows the trend of FoM of non-uniform disc by the viscous actuator disc approach under several different total thrust levels. For each fixed total thrust, the FoM increases first and then decreases with the  $\Delta p_{\text{out}}/\Delta p_{\text{in}}$  rising from a value smaller than 0.5 to roughly 5. The optimal  $\Delta p_{\text{out}}/\Delta p_{\text{in}}$  for maximum FoM resides between 1 and 1.5, which is summarized in Table 3. Recall that the theory predicts the maximum is at 1. It predicts that if a case gives far downstream half the volume flow with  $\Delta p$  up by 20% and half with  $\Delta p$  down by 20% (so the ratio is 1.5), the thrust would be unchanged but the relative power would be  $(1.2^{3/2} + 0.8^{3/2})/2$  and the FoM would therefore be near 0.985. The CFD also fails to reach an FoM equal to 1, plausibly due to its dissipation of kinetic energy; compare with inviscid results presented below. The effect of the pressure-jump level we attribute to different Reynolds numbers, rather than different Mach numbers. Also, with decreasing total thrust, the optimal  $\Delta p_{\text{out}}/\Delta p_{\text{in}}$  moves closer and closer to 1, which agrees with the classical incompressible momentum theory, but the dissipation introduced by numerics in such low speed flow can not be neglected anymore, which could explain the dramatically reduced FoM with the decreasing thrust levels.

Figure 19 compares the development of the wakes in the optimal and uniform cases using VRM. In the optimal case, the inner wake is located in the downwash of the disc and is not strong enough to generate the spiral that appears at the rim. The spiral at the edge is also slightly reduced, and the outer wake crosses the disc slightly closer to the rim. Figure 20 compares the resulting streamlines of viscous actuator disc approach and VRM's two streamlines through  $r/R = 0.7$  and  $r/R = 1$  under  $\Delta p_{\text{out}}/\Delta p_{\text{in}} = 4/3$ . We note also that in the Navier-Stokes solution, no grid refinement was applied where the additional source of vorticity is located, unlike at the rim. Similar to the behavior on the uniform disc, the two methods agree well with the 2 wake streamlines.

Similar to the uniform disc, a finer comparison of the axial and radial velocity components on the disc for  $\Delta p_{\text{out}}/\Delta p_{\text{in}} = 4/3$  are shown in Figure 18 too. The jump of induced radial and axial velocity due to jump of disc loading is well captured by both viscous and inviscid approaches at  $r/R = 0.7$ , although a little overshoot is observed in the VRM, and probably due to the position of the sampling point relative to the closest vortex ring. Compared to the curves of  $\Delta p_{\text{out}}/\Delta p_{\text{in}} = 1$ , the  $V_y$  has a larger region where it is less than  $-V_h$  ( $[0, \sim 0.89R]$ ) and a slightly larger downwash mass flow rate (integral over  $r$ ), which verifies the higher FoM under this non-uniform disc loading condition. Seeing a better FoM with increased load towards the edge of the disc, a good engineer would argue that it makes sense to “move thrust where there is upwash,” in the sense that is a region where the integration in (4) is negative (“upwash” means  $u_z < 0$ ). However, the theory based on the far wake argues that this is compensated by an increased volume flow.

**Table 3 Optimal  $\Delta p_{\text{out}}/\Delta p_{\text{in}}$  and FoM for different induced velocity by solving Navier-Stokes equations.**

$V_h/C_\infty$	optimal $\Delta p_{\text{out}}/\Delta p_{\text{in}}$	optimal FoM
0.05	1.35	0.99994
0.025	1.30	1.00905
0.0125	1.20	0.99063
0.00625	1.13	0.95669

## V. Conclusions and Future Plans

The fluid dynamics of the Actuator-Disc model of rotors, even in its simplest version, are far more complex than could have been expected, especially when applied to a hovering rotor. Propellers with high advance ratios behave more predictably and closely to textbook descriptions, and wind turbines are in-between. Both a viscous approach using an actuator-disc body-force formulation inside the Navier-Stokes equations and an inviscid vortex-ring method are involved into the investigation of the flow over a hovering rotor in the present study.

The actuator disc method with axial pressure jump is numerically studied with different mesh resolution, disc



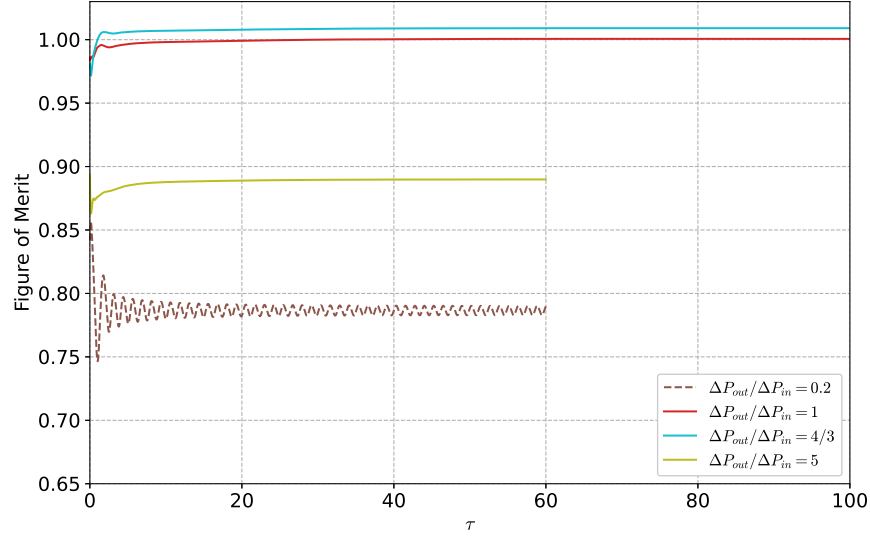


**Fig. 15 Convergence history of Figure of Merit of simulations with the same total thrust ( $V_h/C_\infty = 0.025$ ) but different  $\Delta p_{out}/\Delta p_{in}$**

thickness, different surface shapes and varying disc loading distribution. The following findings were made:

- 1) For CFD simulations using the viscous actuator disc method for initial estimates of loads, using  $0.1\%R$  as grid edge length in the actuator disc region is considered sufficiently fine, because its Figure of Merit only has less than  $0.5\%$  relative error compared to  $0.025\%R$  as grid edge length.
- 2) Different actuator disc thicknesses within the range  $1\%R \sim 4\%R$  show a less than one 0.01 count difference in Figure of Merit.
- 3) With uniform disc loading, the velocity field depends only on the disc rim, and not on the shape of the surface; this was predicted long ago by theory and is relevant to rotor coning or drooping tips. As an exact result, this is limited to the actuator-disc model, but it is a guide for real designs.
- 4) The streamlines and velocity field from the Navier-Stokes solver and from the inviscid approach agree quite well, after making an allowance for the viscous effect on the shear layer. Both methods show a notable upwash velocity at the tip until around  $r/R \approx 0.88 - 0.92$ , again as predicted by theory. The power also agrees quite well.
- 5) Simulations with different pressure jump levels and the Reynolds number kept constant reveal subtle compressibility effects, probably due to details of the solver's operation at very low Mach numbers.
- 6) With non-uniform loading, the  $\left. \frac{\Delta p_{out}}{\Delta p_{in}} \right|_{\text{optimal}}$  that gives the maximum FoM is between 1 and 1.5. With smaller

total thrust and therefore lower Mach number, the FoM shows a convergence trend and the  $\left. \frac{\Delta p_{out}}{\Delta p_{in}} \right|_{\text{optimal}}$  moves closer to 1, which is consistent with the classic incompressible momentum theory. However, this appreciable reduction of the optimal ratio for peak FoM could be due to the numerical dissipation in very low-speed flow, which needs to be investigated in future work.

In summary, the numerical results confirm several features of the rotor flow field predicted by theory which are in strong contrast with textbook presentations going back decades. This is a very positive finding for both theory and CFD. Note that the VRM is best to study the Actuator-Disc flow fields, but would be powerless in real life, which involves non-axisymmetric physics, solid bodies, and so on. Navier-Stokes CFD is ready for that kind of work, although simulating  $360^\circ$  of a rotor and airframe interactions will of course be more challenging than the present situation.

## References

- [1] Spalart, P. R., "On the simple actuator disk," *Journal of Fluid Mechanics*, Vol. 494, 2003, pp. 399–405. <https://doi.org/10.1017/S0022112003006128>.
- [2] Schmidt, G. H., and Sparenberg, J. A., "On the Edge Singularity of an Actuator Disk with Large Constant Normal Load," *Journal of Ship Research*, Vol. 21, No. 02, 1977, pp. 125–131. <https://doi.org/10.5957/JSR.1977.21.2.125>.

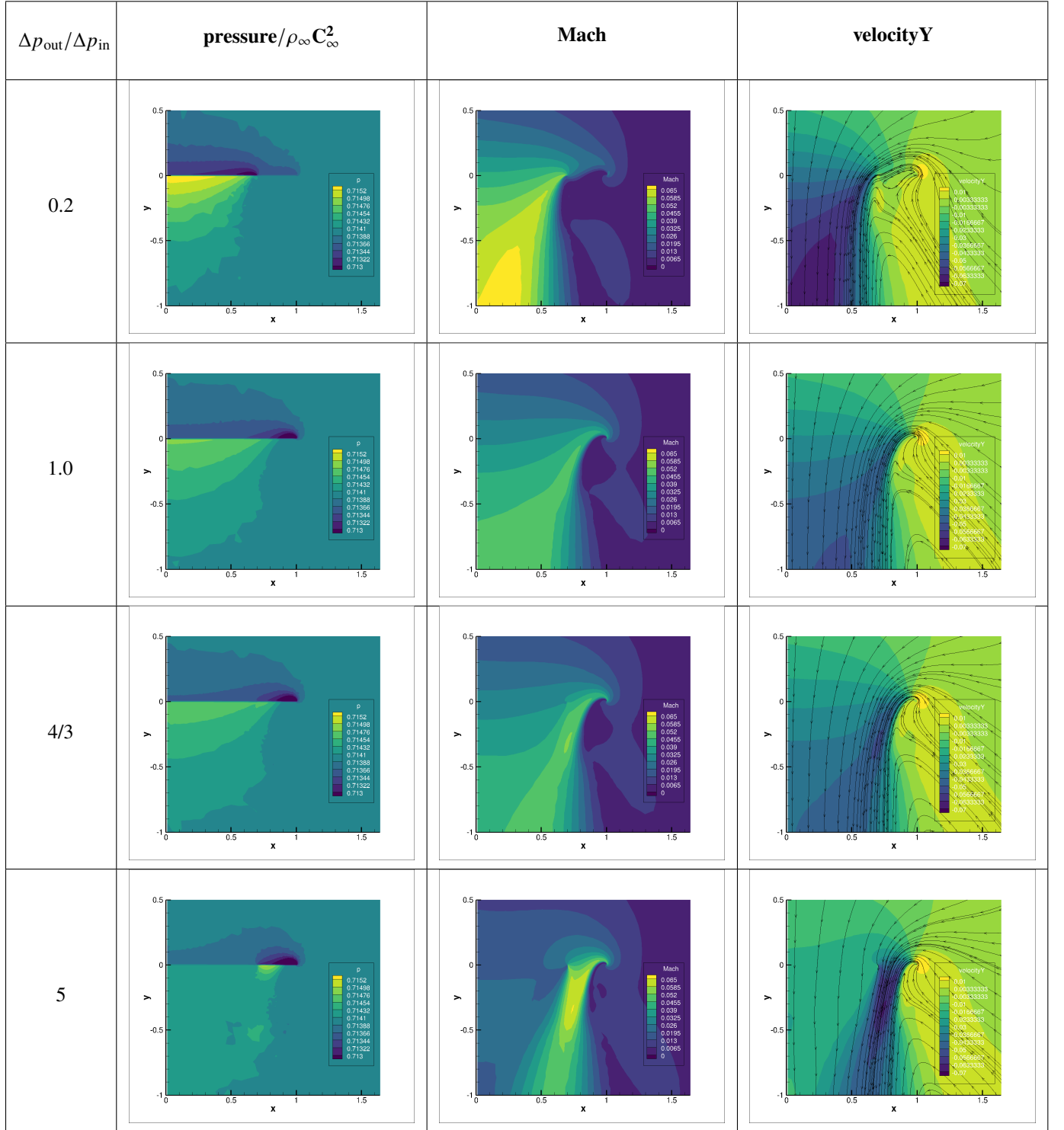


**Fig. 16** Time-averaged flow field comparison of different  $\Delta p_{out}/\Delta p_{in}$  with the same induced velocity  $V_h/C_{\infty} = 0.025$  (flat surface, coarse mesh,  $\epsilon = 2\%R$ ,  $Re = 4e3$ ).

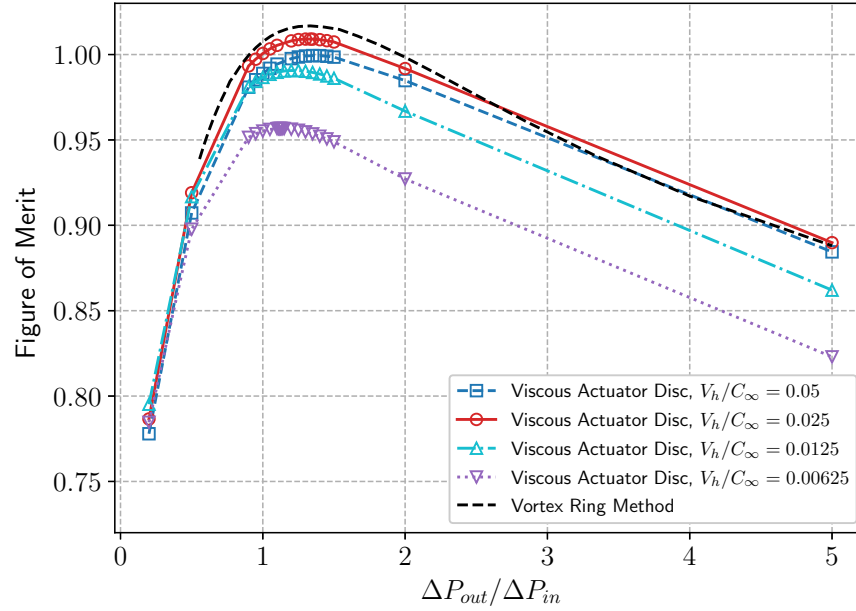
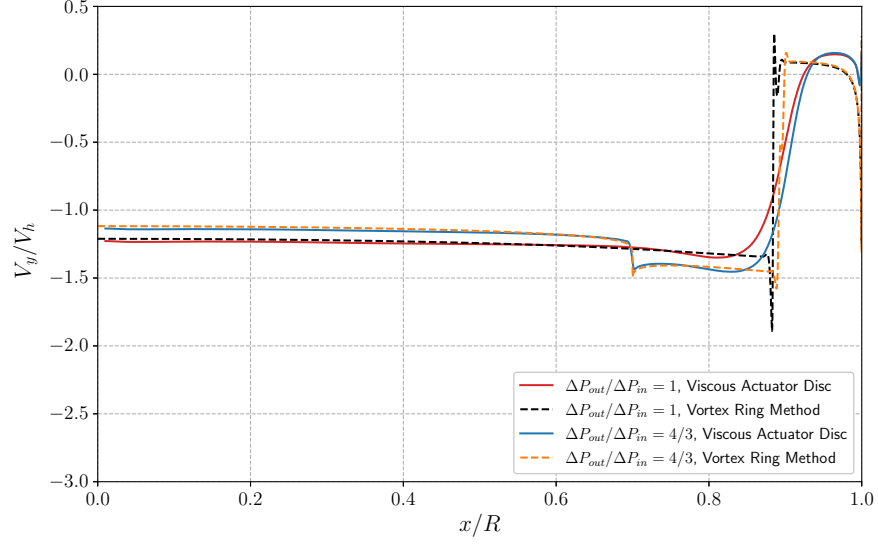
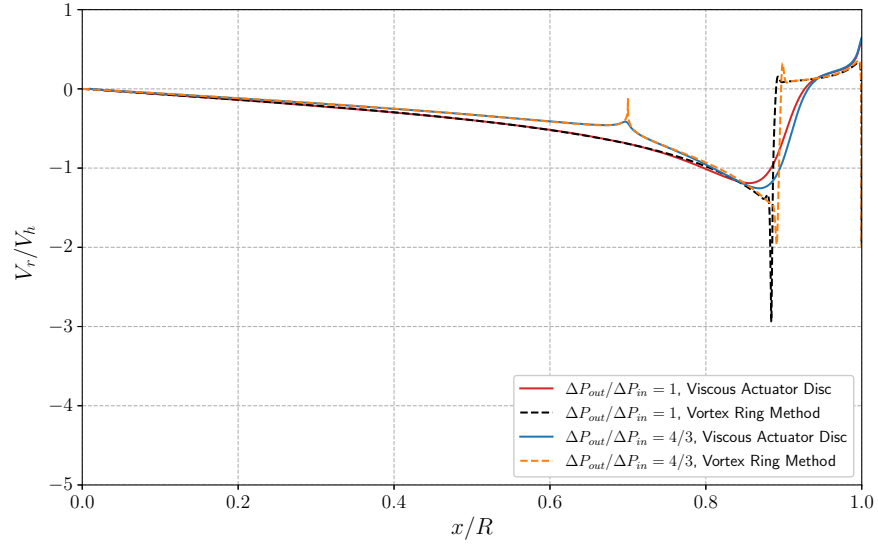


**Fig. 17** Figure of Merit with varying  $\Delta p_{out} / \Delta p_{in}$  (flat surface, coarse mesh,  $\epsilon = 2\%R$ )

- [3] Bontempo, R., and Manna, M., “Optimal Distribution of the Disk Load: Validity of the Betz–Joukowsky Limit,” <https://doi.org/10.2514/1.J061639>, 2022, pp. 1–6. <https://doi.org/10.2514/1.J061639>, URL <https://arc.aiaa.org/doi/abs/10.2514/1.J061639>.
- [4] Gianert, H., “Airplane Propellers,” *Aerodynamic Theory*, Vol. IV, Springer, Berlin, 1935, w. f. durand ed., pp. 169–360.
- [5] Bontempo, R., and Manna, M., “A ring-vortex free-wake model for uniformly loaded propellers. Part II - Solution procedure and analysis of the results,” *Energy Procedia*, Vol. 148, 2018, pp. 368–375. <https://doi.org/https://doi.org/10.1016/j.egypro.2018.08.007>, URL <https://www.sciencedirect.com/science/article/pii/S1876610218302868>, aTI 2018 - 73rd Conference of the Italian Thermal Machines Engineering Association.
- [6] Jia, F., Wang, Q., and Spalart, P., “Improved Initial and Boundary Conditions for Hovering Rotor CFD Simulations,” The Vertical Flight Society Forum 78, Fort Worth, TX, 2022. <https://doi.org/10.4050/F-0078-2022-17474>, URL <https://vtol.org/store/product/improved-initial-and-boundary-conditions-for-hovering-rotor-cfd-simulations-17474.cfm>.
- [7] Spalart, P. R., “On the flow field induced by a hovering rotor or a static jet,” *Journal of Fluid Mechanics*, Vol. 701, 2012, pp. 473–481. <https://doi.org/10.1017/JFM.2012.188>, URL <https://www.cambridge.org/core/journals/journal-of-fluid-mechanics/article/abs/on-the-flow-field-induced-by-a-hovering-rotor-or-a-static-jet/3AAEA48DB3D3C00F5E3D014E27797B84>.
- [8] Dong, J., Viré, A., Ferreira, C. S., Li, Z., and van Bussel, G., “A Modified Free Wake Vortex Ring Method for Horizontal-Axis Wind Turbines,” *Energies*, Vol. 12, No. 20, 2019. <https://doi.org/10.3390/en12203900>, URL <https://www.mdpi.com/1996-1073/12/20/3900>.
- [9] “Archer Midnight (production aircraft),” , 2022. URL <https://evtol.news/archer>.



(a) axial velocity



(b) radial velocity

**Fig. 18** Radial distribution of velocity field at the disc plane obtained by viscous actuator disc approach (flat surface, coarse mesh,  $\epsilon = 2\%R$ ,  $V_h/C_\infty = 0.025$ ,  $Re = 4e3$ ) and VRM with different  $\Delta p_{out}/\Delta p_{in}$ : (a) axial velocity and (b) radial velocity.

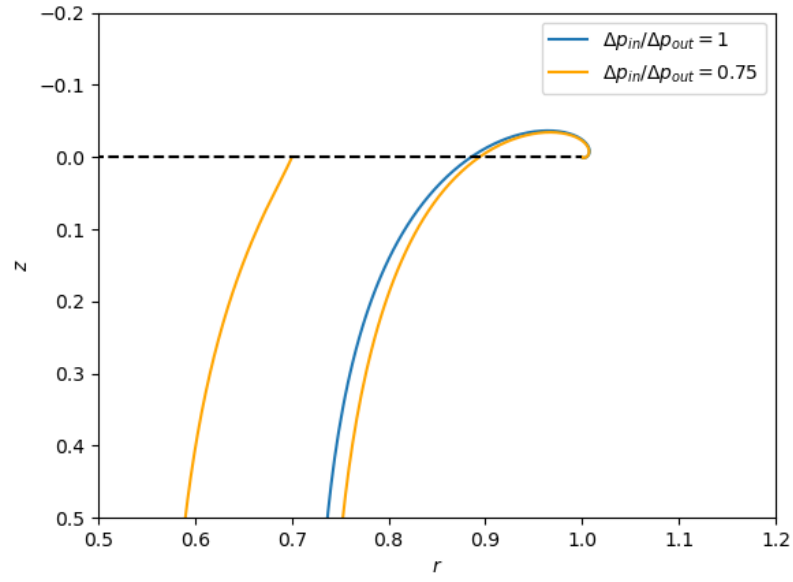


**Fig. 19** Comparison of the wakes near the disc for the uniform loading and the optimal loading ( $\Delta p_{out}/\Delta p_{in} = 4/3$ ) cases using VRM.

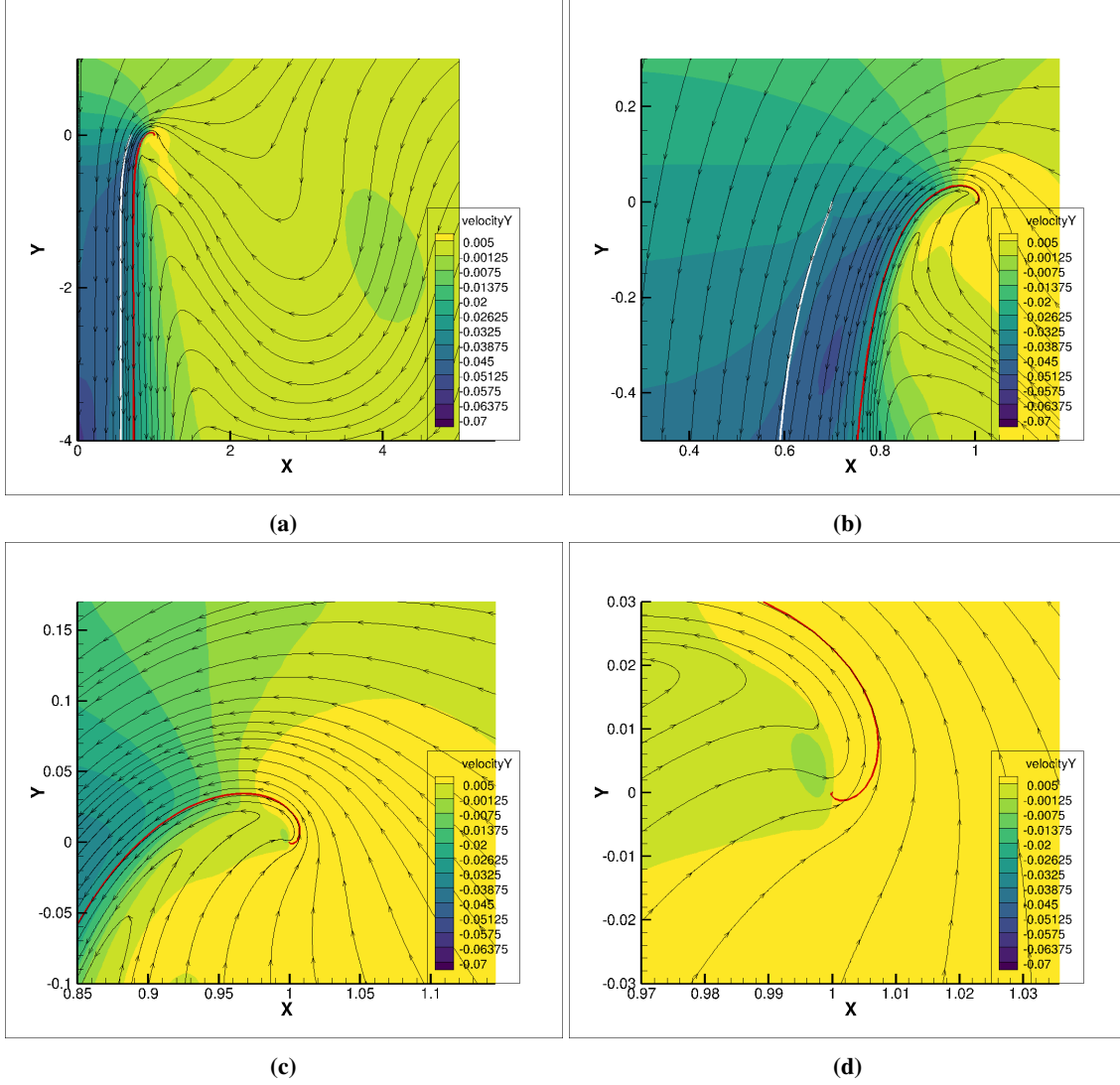


**Fig. 20** Streamlines of flow in non-uniform disc loading,  $\Delta p_{\text{out}}/\Delta p_{\text{in}} = 4/3$ , solved by viscous Actuator Disc approach (arrowed black lines, with flat surface, coarse mesh,  $\epsilon = 2\%R$ ,  $Re = 4e3$ ,  $V_h/C_\infty = 0.025$ ) and inviscid Vortex Ring Method (red line: streamline from  $r/R = 1$ ; white line: streamline from  $r/R = 0.7$ ) in finer and finer zoom levels from (a) to (d). Contour of Y-component of velocity resulting from viscous Actuator Disc approach.